Chapter 4

New Structures of Aluminum Oxide Clusters

4.1 Introduction

Solid Al_2O_3 is a well-studied material with numerous applications. Under normal pressures and temperatures bulk aluminum oxide crystallizes as α-Al_2O_3, better known as corundum. Next to the thermodynamically most stable structure, many metastable A_2O_3 polymorphs, also known as transition aluminas, exist [129–131]. They can be divided into two broad categories: a face-centered cubic or a hexagonal close-packed arrangement of oxygen anions in the crystal. γ-Al_2O_3, θ-Al_2O_3 (monoclinic), and η-Al_2O_3 (cubic) are examples of the former, whereas α-Al_2O_3 (trigonal) and κ-Al_2O_3 (orthorombic) are examples of the latter. Interest in alumina of reduced dimensionality such as small particles or thin films arises from different areas such as astrophysics [132] and atmospheric chemistry [133]. Because of their fine particle size, high surface area, and catalytic activity, the transition aluminas find applications in industry as absorbents [134, 135], catalysts [136] or catalysts support [137–140], coatings [141–147], and soft abrasives [148]. Poorly developed crystallinity and surface reconstruction have made it difficult to advanced surface analytical techniques to probe such fine and irregular structures [129]. Thus, alternative techniques are required to aid in structural characterization of finite aluminum oxide systems.

The vibrational spectroscopy of thin Al_2O_3 films, for example, has been studied by several groups [149–151] finding clear and distinct features caused by lattice vibrations that indicate a γ-Al_2O_3 crystalline structure, i.e., α-Al_2O_3 appears not to be the most stable phase when the dimensions of the alumina material are on the nanoscale. Other useful approaches, which aid in providing insight into the physics and chemistry of the surface [152], are experiments on mass-selected clusters. The finite size of the clusters make it possible to obtain resolved vibrational spectra and to perform higher

level electronic structure calculations. The comparison of the two generally leads to
an unambiguous identification of the geometric and electronic cluster structure, from
which structural motifs and binding information can be extracted. Such information
is particularly important as benchmark data for the more approximative theoretical
models applied to the characterization of surfaces.

Neutral aluminum oxide clusters have been studied by low-temperature matrix
isolation spectroscopy [153–163]. However, these experiments have led to conflicting
and contradictory assignments due to the lack of direct information on the stoichiom-
etry of the absorbing molecular species. Previous gas phase studies on aluminum
oxide ions investigated magnetic properties [164], reactivity [165–169], ionization po-
tentials [170], mass distributions and fragmentation channels [171]. Only few studies
were dedicated to the gas phase spectroscopy of aluminum oxides [152,172–174]. Wang
and coworkers [152] measured photoelectron spectra of small gas phase $Al_xO_y^-$ (x=1,
2, y=1–5) clusters. Based on the vibrationally resolved photoelectron spectra the
ground and excited electronic states of the neutral mono- and dialuminum oxide clus-
ters were revealed and assigned. These clusters are too small to exhibit structural
features of the bulk. Neumark and coworkers [174] measured photoelectron spectra
of the $Al_3O_2^-$, $Al_3O_3^-$, $Al_4O_x^-$, $Al_5O_x^-$ (x=3–5), and $Al_7O_5^-$ clusters. They assigned
structures to the $Al_3O_2^-$ and $Al_3O_3^-$ clusters and their neutral counterparts on the
basis of DFT simulations, but they were unable to resolve any vibrational structure
in the photoelectron spectra of the larger clusters. Van Heijnsbergen et al. [172,173]
measured the infrared resonance-enhanced multiphoton ionization (IR-REMPI) spec-
tra of larger gas phase neutral $AlO \cdot (Al_2O_3)_n$ aluminum oxide clusters ($5 \leq n \leq 70$)
and indeed found preliminary evidence for γ-alumina structures. However they pro-
vided no structural assignment for individual clusters. In the IR-REMPI experiments
cluster ionization, dissociation, and ionization followed by dissociation are all feasible
channels and require comparable energies, complicating the interpretation of the ex-
perimental spectra and making a detailed structural assignment to individual cluster
structures very difficult. Nonetheless, these experiments provided the first, and until
now the only, overview of the IR absorption properties of aluminum oxide clusters
over a large size distribution and over a broad spectral range, yielding a first glimpse
at the size-dependence of characteristic structural motifs in these clusters. For ex-
ample, cluster-size dependent trends were identified and the broad bands they found
at 620 and 900 cm^{-1} were tentatively assigned to structures corresponding to bulk
fcc-structures. Similarly, other studies [175–180] also assumed that small aluminum
oxide clusters have bulk-like structure. However, it is known that gas phase clusters,
in general, and metal oxide clusters, in particular, exhibit structures which may differ
radically from the extended bulk [45].

Here, the spectroscopy of small mass-selected gas phase aluminum oxide clusters
is studied. At first, the IR-PD spectrum of $Al_8O_{12}^+$ is measured and it reveals an
unexpected, non-bulk-like structure. Then, the structural evolution of the closed-shell

$(AlO)(Al_2O_3)_{1-4}^+$ cluster ions is studied as a function of size based on single-photon infrared predissociation spectroscopy.

4.2   Experimental Details

Aluminum oxide clusters are prepared by laser vaporization operated at 10 Hz (see Section 2.1). A mixture of 1% O_2 seeded in He carrier gas is used. At sufficiently low ion trap temperatures (20 K) the formation of aluminum oxide complexes with He and H_2 is observed for the $(Al_2O_3)_{1-4}(AlO)^+$ clusters. These weakly-bound complexes can be exploited to perform *single-photon* vibrational PD experiments (see Section 1.4). For $Al_8O_{12}^+$ neither rare gas nor H_2 complexes are detected. The production of aluminum oxides by laser vaporization is rather unstable. As discussed in Section 1.4.1, this instability is mirrored in the instability of the rare gas complexes yield and it is only partially averaged by the accumulation of many production cycles in the ion trap. In these experiments signal instabilities are on the order of $\sim \pm 10\%$.

For the $(Al_2O_3)_{1-3}(AlO)^+$ clusters, the IR-PD spectra are obtained by monitoring depletion of the messenger complex of the parent ion, i.e., photo-absorption manifests itself as a dip in the ion signal (depletion spectra). For $Al_8O_{12}^+$, the fragment ion $Al_8O_{11}^+$ formation is monitored, and for $(Al_2O_3)_4(AlO)^+$ both depletion of the rare gas complex and the formation of $(Al_2O_3)_4O^+$ (Al loss) are monitored. First, overview spectra with 0.1 µm step size are recorded to identify the absorption regions. Then, the regions of interest are scanned with higher resolution and the appropriate laser attenuation in order to avoid saturation.

4.3   Results and Discussion

A typical mass spectrum of the aluminum oxide cluster cation produced by laser vaporization is shown in Figure 4.1. Although aluminum has no isotopes the mass spectra are quite congested. This is due to the many different oxidation states that aluminum can exhibit. Except for the smaller cluster with two, three, and four aluminum atoms, the most intense peaks are found to have an aluminum/oxygen ratio of (or close to) 2/3 and among these are the ones studied here.

The clusters $(Al_2O_3)_n(AlO)^+$ (n=1–3) appeared to be too strongly bound to be fragmented by IR multiple photon dissociation with the available FELIX energy of $\sim$50 mJ. For $(Al_2O_3)_4^+$ no rare gas complexes can be detected. The fact that multiple photon dissociation cannot be achieved for the n=1–3 clusters, while they create the rare gas complexes is by itself an interesting result. It means that these complexes must be strongly bound (and this fact is mirrored by the high abundances in the mass spectrum) and that the positive charge must be localized, as discussed in Section 1.4.
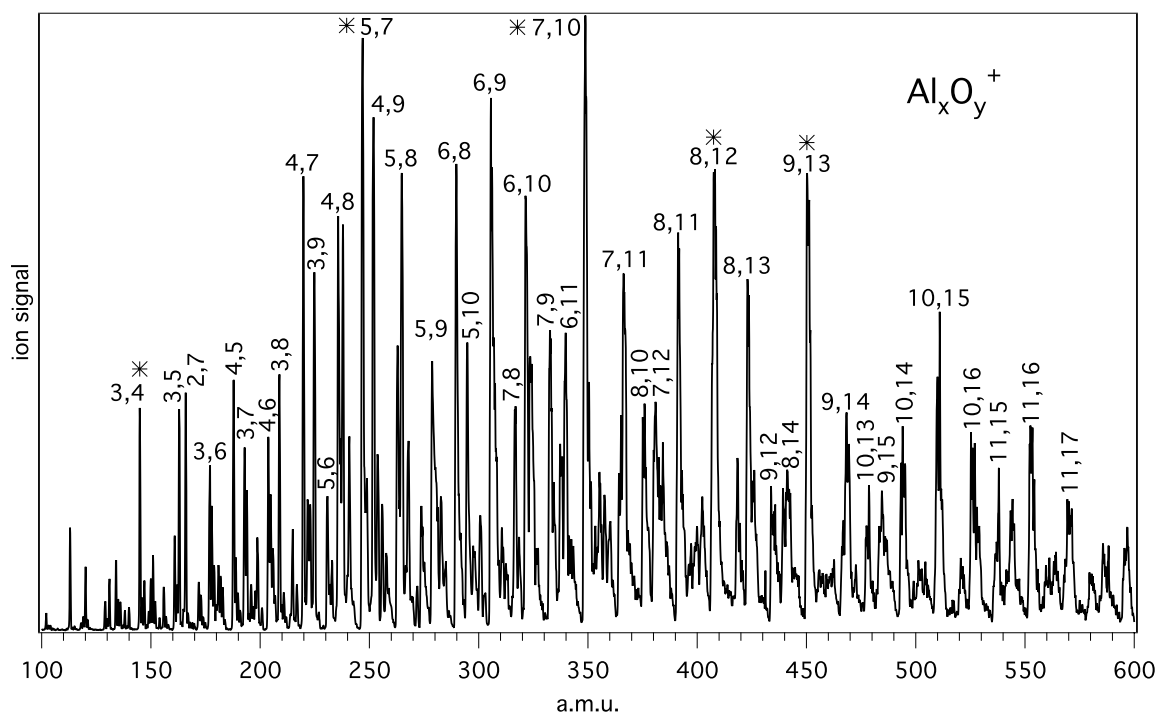
Figure 4.1: A typical mass spectrum of aluminum oxide cations produced by laser vaporization. The spectrum is congested by the many possible oxidation states of aluminum. The most intense peaks are identified as (x,y) for the clusters $Al_xO_y^+$. The measured clusters are marked with an asterisk.

To assist the structural assignment DFT geometry optimization were carried out in the Sauer group (Humboldt-Universität zu Berlin, Germany). Atomic structures were found by combining density functional theory (DFT) and experiment, but only after implementing a genetic algorithm as global optimization technique [181–183]. DFT calculations were done using the TURBOMOLE program [118], employing the B3LYP hybrid functional [119] and the TZVP basis sets [120].

4.3.1 $(Al_2O_3)_4^+$

The experimental IR-PD spectrum of $(Al_2O_3)_4^+$, obtained monitoring $Al_8O_{11}^+$ formation (oxygen loss) is shown in Figure 4.2 (top panel). The most intense absorption band is at 997 cm^{-1} with a clear shoulder at 1024 cm^{-1}. At least five bands are found between 700 and 950 cm^{-1} and a less intense but broad feature is visible around 640 cm^{-1}.

The topology of the $(Al_2O_3)_4$ cluster is described in the literature [175–180] as characterized by n-membered rings consisting of alternating Al and O atoms, denoted

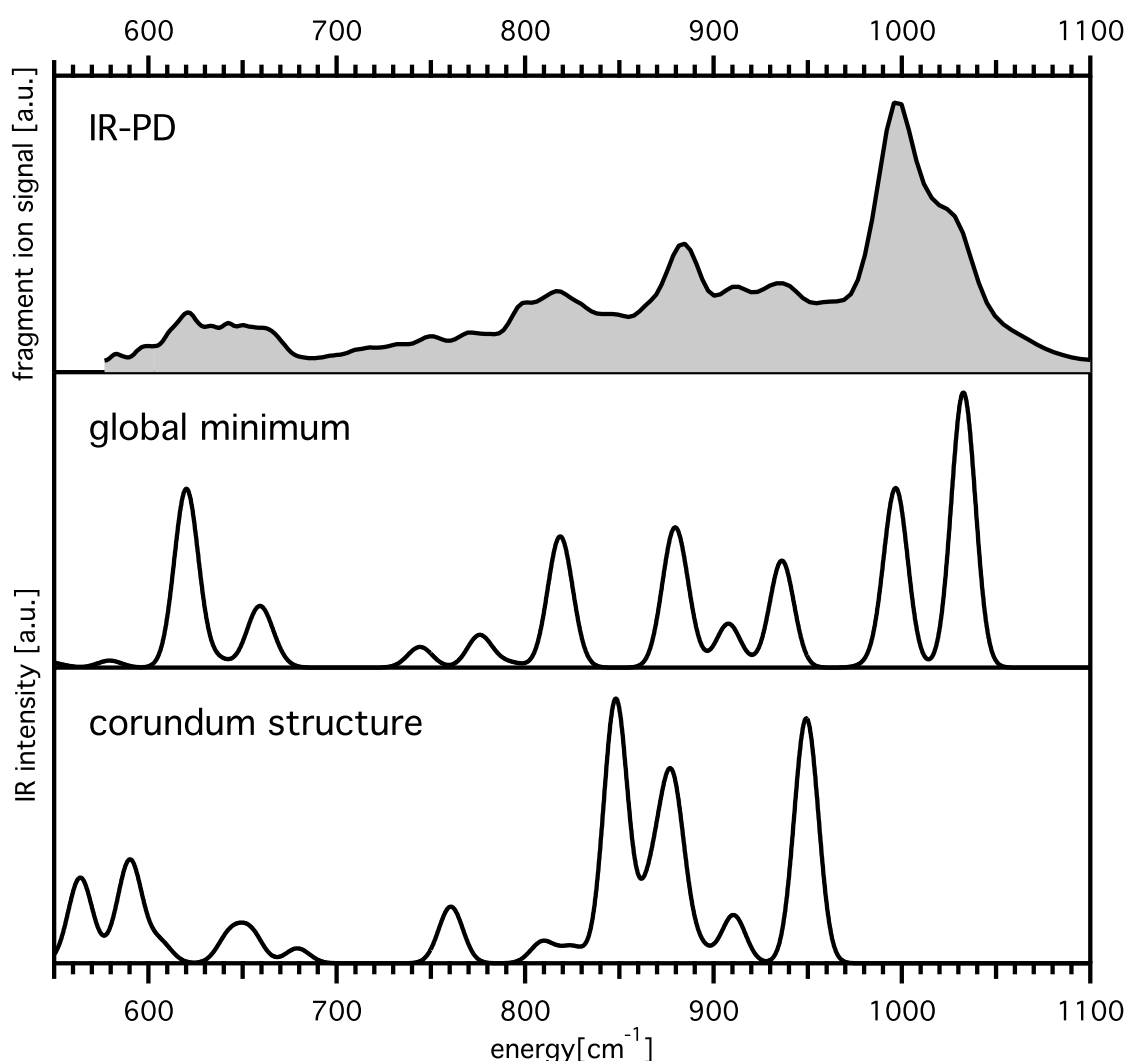**Figure 4.2:** Comparison of experimental IR-PD spectrum of $(Al_2O_3)_4^+$, obtained monitoring $Al_8O_{11}^+$ formation (top), and calculated IR absorption spectra of global minimum $(Al_2O_3)_4^+$ (center). The calculated IR absorption spectrum of α-$(Al_2O_3)_4^+$ is reported on bottom for comparison.

as nm rings. The compact structure of the neutral $(Al_2O_3)_4$ corundum fragment (Figure 4.3), denoted α-$(Al_2O_3)_4$ hereafter, consists of 6m and 4m rings only. There are six fourfold and two threefold coordinated Al atoms in the cluster as well as six twofold and six threefold coordinated O atoms, with Al$-$O bond distances in the range of 1.71–1.91 Å. DFT calculations find this structure to be stable both in the neutral and in the cationic state, in agreement with previous works [175–180]. In the cationic state the D_{3d} symmetry of the neutral α-$(Al_2O_3)_4$ cluster is lowered to C_s

due to the first order Jahn-Teller effect. However, the distortion is relatively small and the main structural features remain unchanged. In the lower part of Figure 4.2
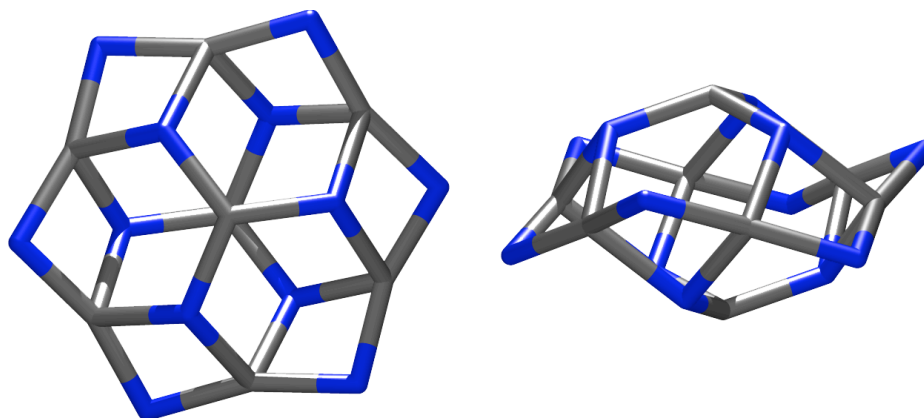

Figure 4.3: Bulk like structure of $(Al_2O_3)_4$ derived from the corundum lattice.

the calculated spectrum for $\alpha\text{-}(Al_2O_3)_4^+$ is plotted for comparison. It is clear that the $\alpha\text{-}(Al_2O_3)_4^+$ is not the observed structure, because the most intense band in the experimental spectrum around 1000 cm^{-1} is not reproduced by the calculations.

The global optimization of the cationic $(Al_2O_3)_4^+$ cluster employing the genetic algorithm yields a C_s symmetric structure with an "arrowhead" shape shown in Figure 4.4. It is about 125 kJ/mol more stable than the $\alpha\text{-}(Al_2O_3)_4^+$ cluster at the B3LYP level. The base of the arrowhead is formed by five fused 6m rings forming a 10m ring at the bottom and a 6m ring at the top. An additional O atom at the top of the chain of fused 6m rings forms three fused cube fragment-like 4m rings. One additional O atom is coordinated to the top-most Al apex of the cube fragment, forming the tip of the arrowhead. The cluster contains three fourfold and five threefold coordinated Al atoms as well as seven twofold, four threefold, and one single coordinated O atom. The Al−O bond distances are in a range of 1.69–1.87 Å, with the shortest ones (1.69–1.73 Å) in the 10m ring at the arrowhead base. The Al−O distance of the singly coordinated O atom at the tip is 1.74 Å.

Figure 4.2 shows the experimental IR-PD (top) and the calculated linear absorption spectra for the global minimum $(Al_2O_3)_4^+$ (center). The spectrum of the global minimum structure shows excellent agreement with the experiment. It reproduces all observed vibrational bands, albeit with slightly different intensities. Deviations between the IR-PD and linear absorption spectra are not unexpected as discussed in Chapter 1. Specifically, the experimental spectrum shows a characteristic vibrational band at about 1030 cm^{-1}. This unusual high frequency band is not known for any bulk Al_2O_3 phase. One may assume that it belongs to a mode that involves stretching of a terminal Al−O bond. However, the analysis of the vibrational modes of the global minimum $(Al_2O_3)_4^+$ cluster shows that this fingerprint vibration is an
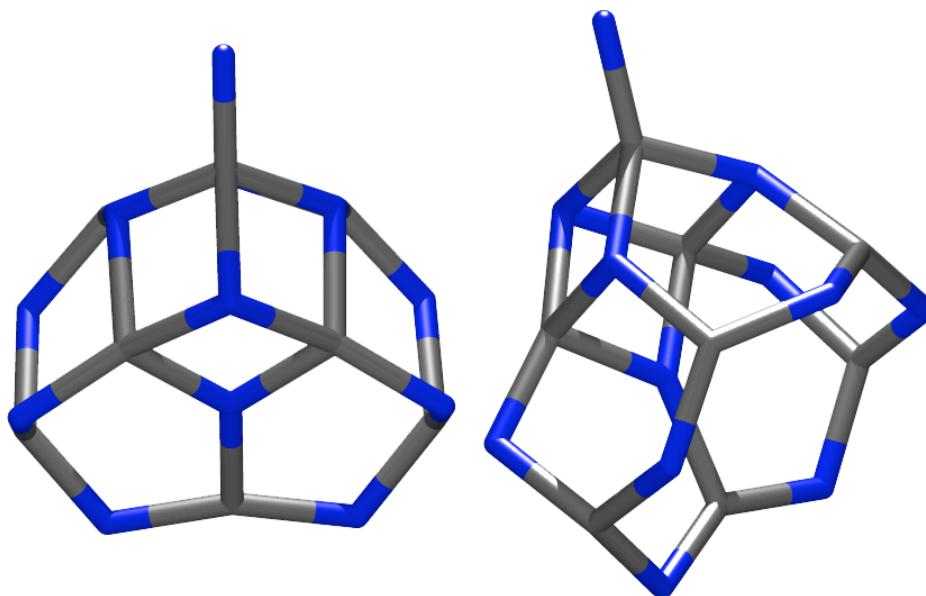
Figure 4.4: Global minimum structure of $(Al_2O_3)_4^+$ calculated by Sauer and coworkers.

out-of-phase coupling of the asymmetric Al−O−Al stretching vibrations shown in Figure 4.5, while the stretching vibration of the terminal Al−O bond is located at about 870 cm^{-1}. Interestingly, out of dozens of calculated $(Al_2O_3)_4^+$ structures this vibration is reproduced only for the global minimum structure.

The question arises what the driving force is that causes the $(Al_2O_3)_4^+$ cluster to assume this unusual arrowhead shape with one singly coordinated O atom. The answer is provided by the calculated spin density distribution, which shows that the single unpaired electron as well as the positive charge are fully localized at the singly coordinated tip O atom, making the terminal bond formally an Al−O single bond (see Figure 4.6 left). This explains the unusually low frequency of the corresponding stretching vibration. Electrostatic interactions must then be the driving force responsible for the arrowhead shape of the cluster since such a remarkable positive charge localization is not possible in the α-$(Al_2O_3)_4^+$ cluster.

Schwarz and coworkers [184] have recently provided the first example of thermal activation of methane by a polynuclear transition-metal oxide. This observation is not trivial, because the often extremely reactive mononuclear metal oxides are not ideal model systems relevant for an understanding of a real-life oxidation catalyst; larger systems, that is, cluster oxides, are better suited to serve this purpose. In particular they found that in the radical cation $V_4O_{10}^+$ one valence electron is missing from one V=O bond, leading to an elongation of the vanadyl bond. The spin density has the shape of a p orbital and is mainly localized at the vanadyl oxygen atom (see Figure 4.6
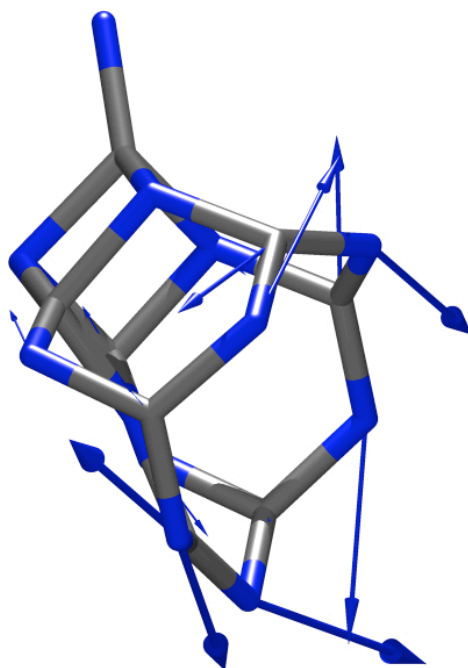
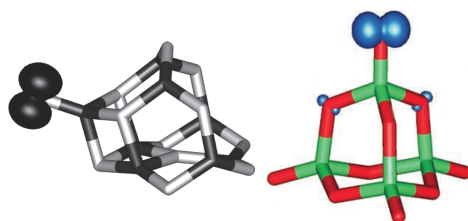**Figure 4.5:** A schematic drawing of the fingerprint vibrational mode at 1030 cm^{-1}.

Figure 4.6: Calculated spin density for $(Al_2O_3)_4^+$ (left) and $V_4O_{10}^+$ (right) from Ref. [184].

right). The similarity of this spin density to the one calculate for $(Al_2O_3)_4^+$ proposes $(Al_2O_3)_4^+$ as a candidate for further reactivity studies.

4.3.2 $(Al_2O_3)_{1-4}(AlO)^+$

Mass spectra obtained after trapping mass-selected $(Al_2O_3)_n(AlO)^+$ clusters for tens of milliseconds at 20 K and then extracting all ions into the second quadrupole mass filter are shown in Figure 4.7. The largest peak in the spectrum corresponds to the (bare) parent ion, which was initially selected in the first quadrupole mass filter, and is labeled "Parent" on the mass axis. Additional peaks are observed at masses larger than that of the parent ion. These peaks are assigned to complexes of the parent
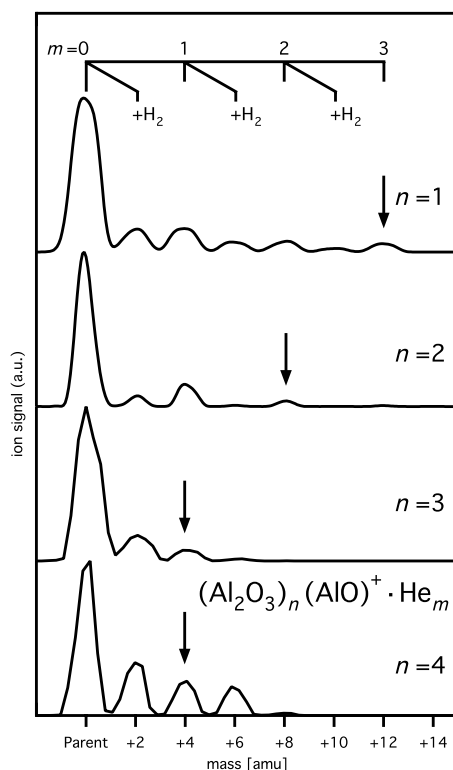
Figure 4.7: Mass spectra obtained after trapping $(Al_2O_3)_n(AlO)^+$ clusters with n=1–4 (top to bottom) for several tens of milliseconds at 20 K and then extracting all ions from the ion trap into the second mass filter. For an easier comparison all mass spectra are aligned to the mass of the corresponding parent ion, which is initially mass-selected using the first mass filter. The mass channels, which were used to monitor the IR-PD spectra in 4.8, are indicated by arrows.

ion with He atoms, H_2 molecules or both (see also Ref. [54]). Next to He, traces of H_2, the main component of rest gas degasing from the machine walls, is also present in the trap region. Even though H_2 is present at much lower concentration than He, it competes in the formation of complexes due to its higher polarizability and thus binding energy. The presence of H_2 makes the assignment of the mass spectra less straight-forward, because of $2\mathcal{M}(H_2)=\mathcal{M}(He)$, where $\mathcal{M}(He)$ and $\mathcal{M}(H_2)$ are the masses of a helium atom and a hydrogen molecule, respectively. However, for n=1 and n=2 the intensity distributions do suggest a dominant $\Delta\mathcal{M}$=4 amu progression with m=1–3, where m is the number of He atoms, (see Figure 4.7) and weaker peaks in-between for $\Delta\mathcal{M}$=2 amu. This corresponds to the predominant formation of pure He complexes and to a lesser extent bare and He-containing complexes with a single H_2 molecule. In order to minimize the contribution of H_2 containing complexes IR-PD

spectra are measured by monitoring the depletion of the peak corresponding to the largest He complex observed in the mass spectrum with sufficient signal, i.e., $m=3$ for $n=1$, $m=2$ for $n=2$, and $m=1$ for $n=3$ and 4. This also minimizes contributions from other ions decaying into the monitored mass channel. However, for $n=3$ and $n=4$ there may be, indeed, a significant contribution from the complex containing two H_2 molecules.

The IR-PD spectra of $Al_3O_4^+$, $Al_5O_7^+$, $Al_7O_{10}^+$, and $Al_9O_{13}^+$, measured by monitoring the depletion of a corresponding messenger complex as described, are shown in Figure 4.8 together with the calculated linear absorption spectra of the most stable structures. Observed peak positions are listed in Table 4.1. As already mentioned above, the stability of the production of aluminum oxides by laser vaporization was on the order of $\pm 10\%$ of the signal leading to small variations in the parent ion baseline.

The experimental IR-PD spectrum of $Al_3O_4^+\cdot(He)_3$ (Fig. 4.8A) is rather simple. It shows a very strong absorption at 871 cm^{-1}, a group of four maxima around 700 cm^{-1}, and two less intense bands at 602 and 543 cm^{-1}. The spectrum of $Al_5O_7^+\cdot(He)_2$ (Fig. 4.8B) is more complex. It shows three main absorption regions. Next to the bands observed around 850 and 750 cm^{-1}, two additional intense peaks are found at 1004 and 980 cm^{-1}, more than 100 cm^{-1} higher in energy than the highest absorption in $Al_3O_4^+\cdot(He)_3$. The IR-PD spectra of the two larger species, $Al_7O_{10}^+\cdot(He)$ and $Al_9O_{13}^+\cdot(He)$ (or the corresponding H_2 complexes), are considerably more complex, showing absorptions in the complete spectral region studied between 550 and 1050 cm^{-1}. The most significant trend observed in these spectra is a monotonic blue shift of most intense band from 871 cm^{-1} for $n = 1$ to 1029 cm^{-1} for $n = 4$.

The lowest energy structure calculated for $Al_3O_4^+$ has C_{3v} symmetry and consists of a 6-membered (6m) ring of alternating Al and O atoms and an O atom at the top of the ring (see Figure 4.9A). All Al atoms and one O atom are threefold coordinated and the other three O atoms are twofold coordinated. The calculated linear IR absorption spectrum (see Figure 4.8A) is in excellent agreement with the experimental IR-PD spectrum with respect to peak positions and relative peak intensities. The most intense band, calculated at 867 cm^{-1}, and found at 871 cm^{-1} in the experiment, corresponds to a degenerate mode involving the atoms of the 6m ring (see Figure 4.11). The three absorptions found at 750, 722, and 700 cm^{-1}, calculated at 751, 712, and 696 cm^{-1}, on the other hand, result from modes involving the complete cluster, i.e., they also involve the three fold coordinated oxygen atom. Finally, the bands at 678, 602, and 543 cm^{-1} correspond to vibrations (696, 601, and 538 cm^{-1}) involving mainly the threefold coordinate oxygen atom.

The lowest energy isomer calculated for $Al_5O_7^+$ has C_s symmetry and consists of three 6m rings and one 4m ring, adjacent to each other, forming a 8m ring (see Figure 4.9B). All aluminum atoms and one oxygen atom are threefold coordinated, while the remaining oxygen atoms are twofold coordinated. The complete experimental spectrum from 700 to 1000 cm^{-1} is accurately reproduced by the calculations. The
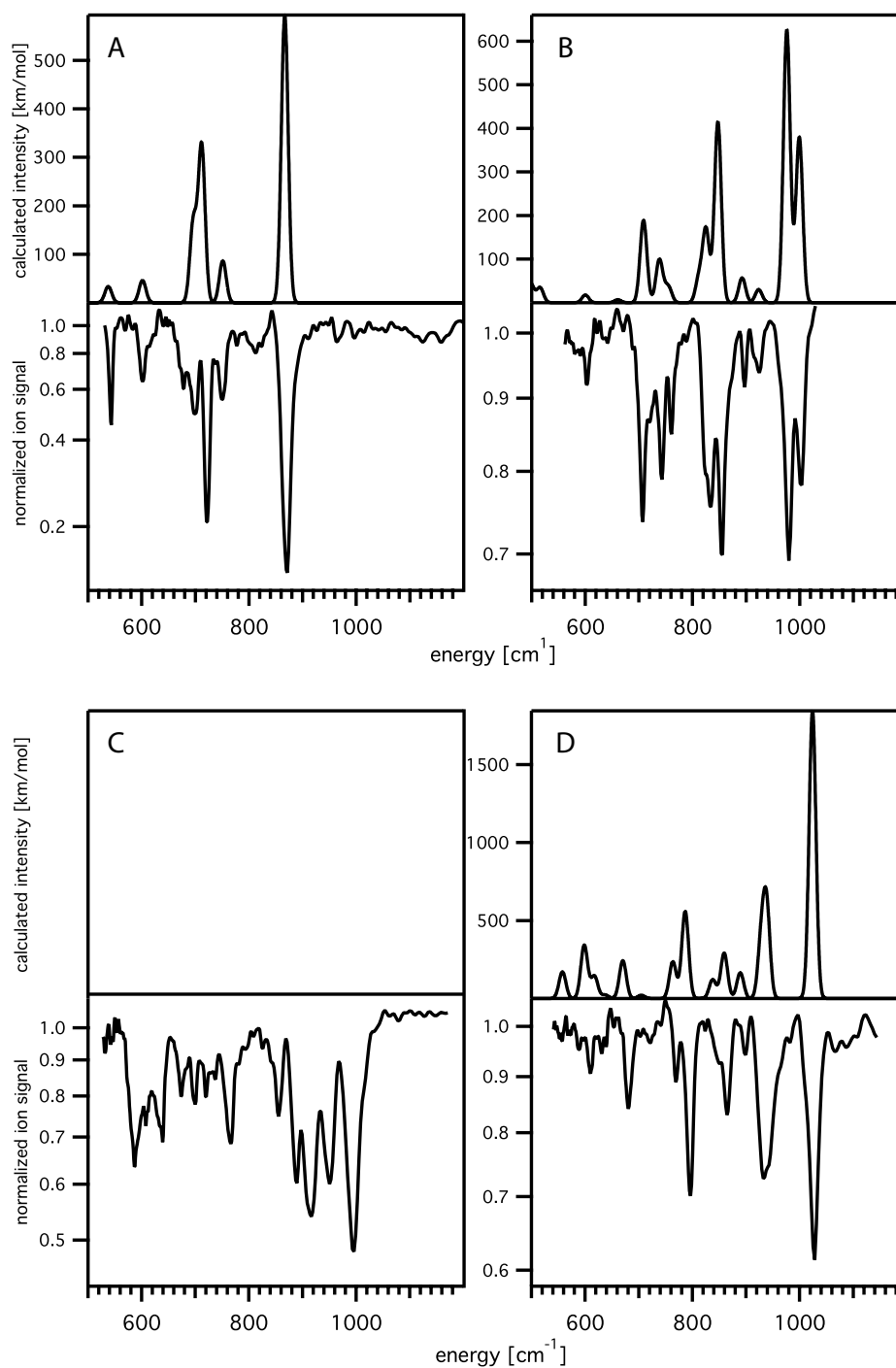
Figure 4.8: IR-PD spectra (bottom) together with the calculated linear absorption spectra of the most stable structures (top) of $Al_3O_4^+\cdot(He)_3$, $Al_5O_7^+\cdot(He)_2$, $Al_7O_{10}^+\cdot(He)$, and $Al_9O_{13}^+\cdot(He)$, A to D, respectively. Calculations for $Al_7O_{10}^+$ are not yet available.

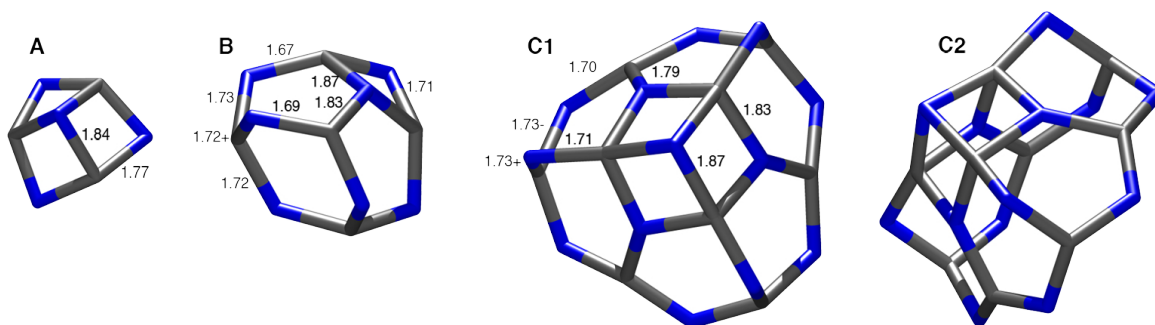**Figure 4.9:** The most stable structures for the $(Al_2O_3)_n(AlO)^+$ clusters, with $n=1$ (A), 2 (B), and 4 (C1 and C2). Bond lengths are expressed in Å.

Parent Ion	Fragment	Position of Observed Bands (cm^{-1})
$Al_3O_4^+ \cdot (He)_3$	depletion	870, 749, 721, 699, 690(s), 678, 672(s), 602, 543
$Al_5O_7^+ \cdot (He)_2$	depletion	1022(s), 1004, 980, 927, 915, 897, 856, 832, 824(s), 761, 741, 721(s), 707, 641, 604
$Al_7O_{10}^+ \cdot (He)$	depletion	1015(s), 993, 951, 919, 890, 856, 824, 770, 738, 721, 701, 673, 639, 608, 588
$Al_8O_{12}^+$	$Al_8O_{11}^+$	1024, 997, 937, 913, 885, 849(s), 817, 801(s), 771, 751, 662(s), 642, 622, 601, 584
$Al_9O_{13}^+ \cdot (He)$	depletion	1032, 965, 946, 935, 899, 867, 851(s), 836, 818, 798, 769, 723, 715, 679, 631, 603, 556, 536
$Al_9O_{13}^+$	$Al_8O_{13}^+$	1035, 1003, 979, 930, 902, 890, 832, 814, 797, 780, 747, 717, 670, 657, 627, 604, 549

Table 4.1: Experimental vibrational frequencies (in cm^{-1}) of aluminum oxide cluster cations determined from the respective IR-PD spectra. Vibrational frequencies are determined from band maxima or estimated based on observable shoulders (s) formed by overlapping transitions.

two highest energy modes calculated at 999 and 976 cm^{-1}(exp.: 1004 and 980 cm^{-1}) involve the motion of all atoms from the 8m ring (see Figure 4.11). Such a ring is not present in the smaller cluster and consequently $Al_3O_4^+$ does not absorb in the region above 900 cm^{-1}. The threefold coordinated oxygen atom is mainly involved in the motion that accounts for the 709 cm^{-1} peak (exp.: 707 cm^{-1}). Below 700 cm^{-1} the agreement is less satisfactory. While the position of most intense feature in this region at 604 cm^{-1} is well reproduced (calc.: 600 cm^{-1}), additional minor features are observed in the experimental spectrum, which are not accounted for by the calculations.

Calculations find a second isomer close in energy (+1.2 kJ/mol) to the most stable one whose agreement with the experimental data is worse. In particular, the intensity of the calculated mode at 896 cm^{-1} is not compatible with the experiment, as well as the absence of any feature around 820 cm^{-1}; of the three peaks measured around 750 cm^{-1} only two are calculated to have sufficient intensity. Clearly, this isomer cannot exclusively account for the experimental one. However, taking the calculated energetics into consideration this second isomer may give a minor contribution to the experimental spectrum. Assuming both isomers are present, the best fit to the experimental spectrum is obtained for a ratio of 75:25 (see Figure 4.10).

No calculations are available for $Al_7O_{10}^+$. The IR-PD spectrum of $Al_7O_{10}^+$ shows the most intense band at 993 cm^{-1}. Three bands around 900 cm^{-1} and several absorptions in the whole region between 550 and 850 cm^{-1} are found. The congestion of the spectrum may suggest that more than one isomer is present in the ion beam.

The lowest energy isomer calculated for $Al_9O_{13}^+$ has C_{3v} symmetry and consists of six 6m adjacent rings, forming a 12m ring on one side and a 6m ring on the other (see Figure 4.9C). Atop of the 6m ring there is a threefold coordinated oxygen atom (building a substructure similar to $Al_3O_4^+$). Four oxygen atoms located in the center of the cluster are threefold coordinated while the other nine are twofold coordinated. Three aluminum atoms in the center of the cluster are fourfold coordinated while the other six are threefold coordinated. Again, a very good agreement between experiment and calculations is found. The most intense mode (degenerate), that is also the one at highest energy, at 1024 cm^{-1} (exp.: 1029 cm^{-1}), is due to the motion of atoms of the 12m ring (see Figure 4.11). The mode at 939 cm^{-1} (exp.: 935 cm^{-1}) involve the vibration of the O atoms belonging to the 6m rings. The vibrations involving the central oxygen atom are calculated at 637, 598, and 558 cm^{-1} and the experiment find maxima at 631, 610, 590, and 558 cm^{-1}. Considering the relative intensity, the measured 631 cm^{-1}-band can tentatively be assigned to the calculated 637 cm^{-1}-mode, the 610 cm^{-1}-band to the 598 cm^{-1}-mode, and the 558 cm^{-1}-band to the 558 cm^{-1}-mode.

Among the studied clusters, $Al_9O_{13}^+$ is the only one for which both helium complexes and photodissociation of the bare cluster are observed. After trapping $Al_9O_{13}^+$, both the bare ion and the helium complex are present in the trap (see Figure 4.7), thus it is possible to measure the multiple photon IR-PD spectrum by recording the
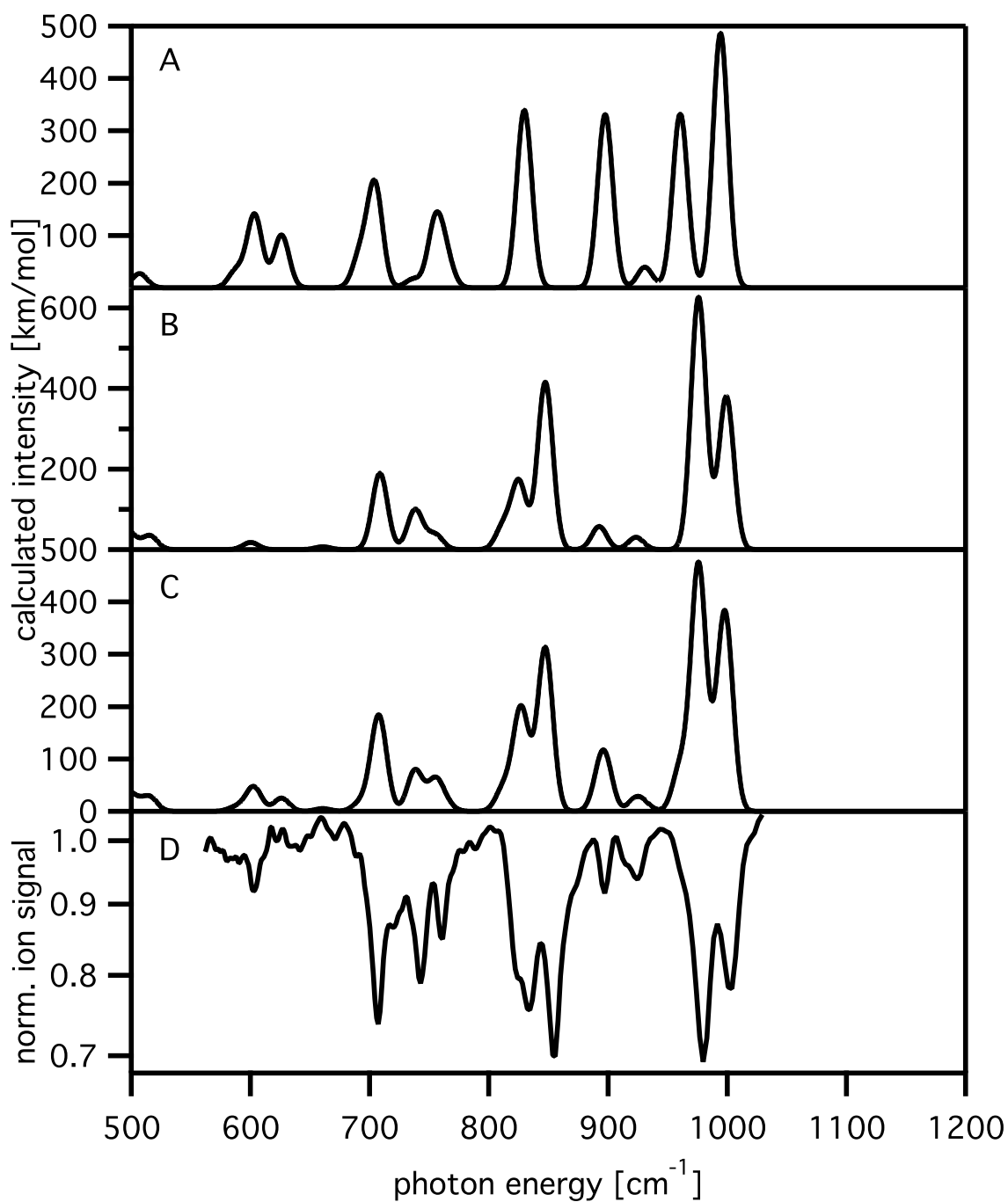
Figure 4.10: IR-PD spectrum (D) of $Al_5O_7^+ \cdot (He)_2$. The calculated linear absorption spectra of the most stable isomer (B), of the second most stable, +1.2kJ/mol (A), and of a mixture of the two isomers in a 75:25 ratio (C).
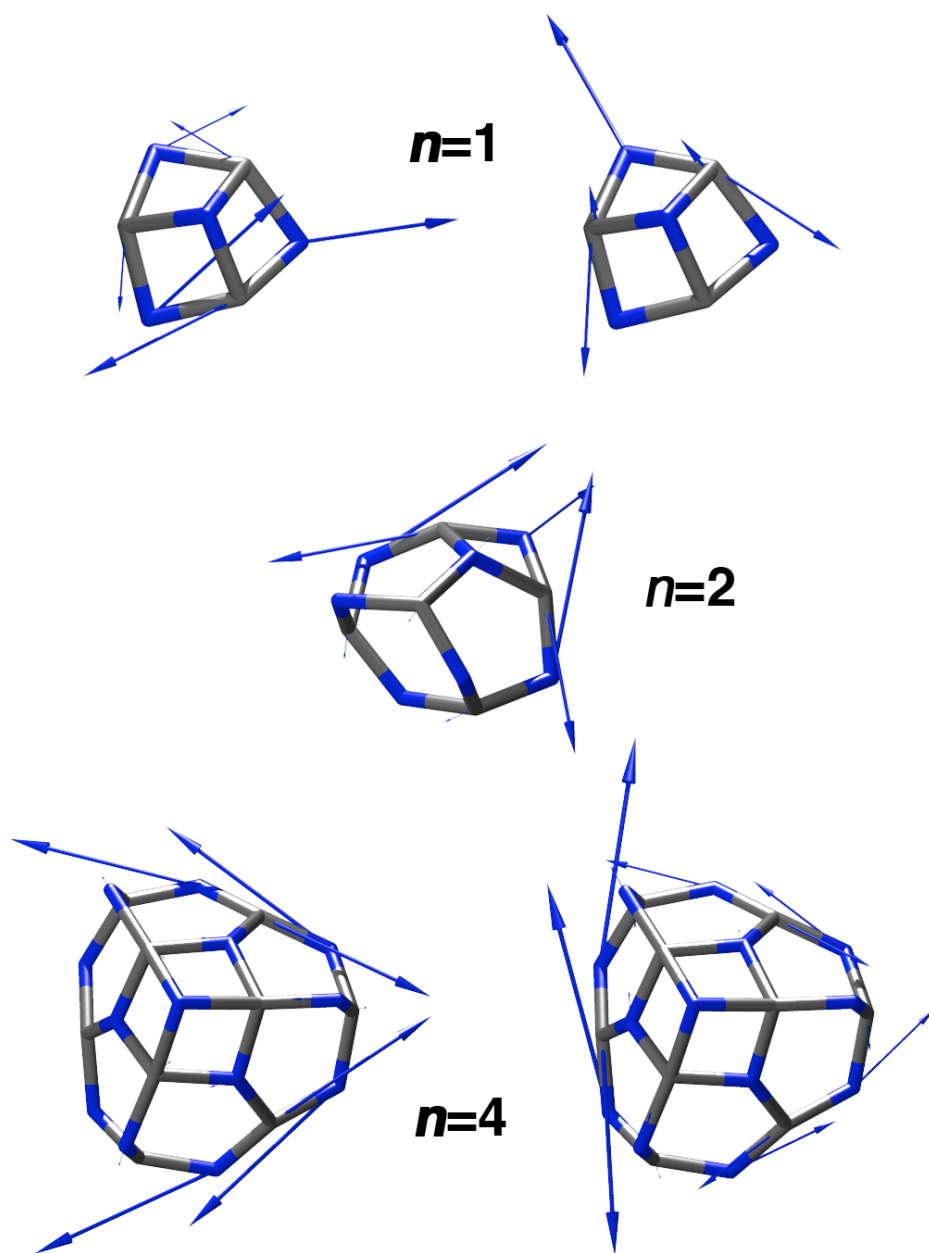
Figure 4.11: Schematic drawings of the fingerprint vibrational modes for the n=1, 2, and 4 clusters. For n=1, the two degenerate modes calculated at 867 cm^{-1} are shown; they involve the motion of the 6m ring atoms. For n=2, the highest energy mode calculated at 999 cm^{-1} is shown; it involves the motion of the 8m ring atoms. For the n=4, the two degenerate modes calculated at 1024 cm^{-1} are shown; they involve the motion of the 12m ring atoms.
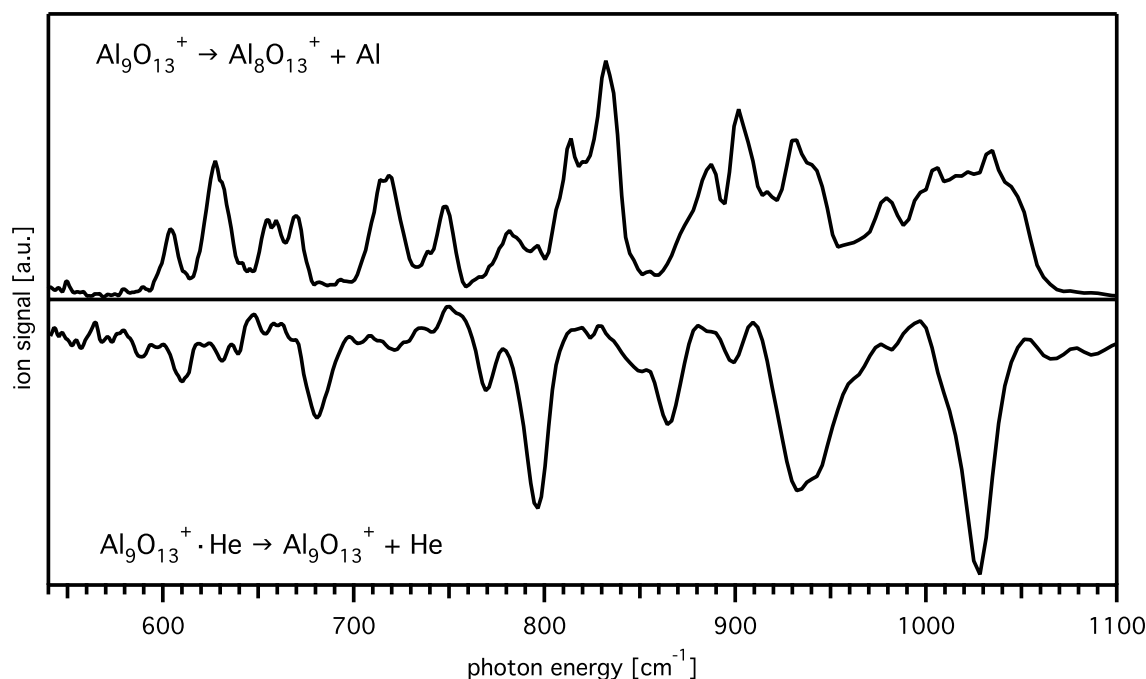
Figure 4.12: IR-PD spectra of $Al_9O_{13}^+$. The multiple photon IR-PD (top) is measured by recording the fragment $Al_8O_{13}^+$ ion formation (Al-loss). The single photon IR-PD (bottom) is measured at the same time monitoring the $Al_9O_{13}^+\cdot$He complex depletion.

fragment $Al_8O_{13}^+$ ion yield (aluminum loss) and the single photon IR-PD spectrum by monitoring the $Al_9O_{13}^+\cdot$He complex depletion in dependence on FELIX wavelength. To do so, the measurement cycle is repeated for every wavelength step, setting the the second mass filter (Q3) once to the $Al_8O_{13}^+$ mass and once to the $Al_9O_{13}^+\cdot$He mass. Note that FELIX is not tuned between the two measurement cycles so that the points of the two spectra are recorded exactly at the same wavelengths. The two IR spectra are shown in Figure 4.12. They have a similar number of bands distributed over the whole spectra region between 500 and 1100 cm^{-1}, but in different positions. The $Al_8O_{13}^+$ fragment yield is $\sim$5% of the $Al_9O_{13}^+$ parent at 832 cm^{-1}, the absolute maximum in the spectrum. The spectra are measured with strong FELIX attenuation (-8 dB) to avoid saturation of the signal. Increasing FELIX power broadens the bands and reduces the $Al_9O_{13}^+\cdot$He yield to zero on top of the absorption bands but it neither increases significantly the signal yield of the $Al_8O_{13}^+$ fragment nor it changes the position of the bands. The two different spectra are, therefore, probably due to different isomers present in the trap. The first is more strongly bound and its charge is more localized so that it does not fragment even under the unattenuated FELIX pulses but it does create complexes with helium atoms. The second is less

strongly bound and its charge is less localized so that it easily fragments, but it does not create helium complexes. Moreover, only a small fraction of the ions in the trap consists of the the second isomer, given the little fragment yield and its negligible power dependence (whereas in other systems either fragment yields up to 80% of the parent signal are observed or the available light power is the limiting factor for the observed fragment yields, see Chapter 3, for example). Unfortunately, no calculations are available that can account for the second isomer.

4.4 Summary

In this study, IR-PD spectra for $(Al_2O_3)_n(AlO)^+$ with n=1–4, and for $(Al_2O_3)_4^+$ have been measured. Structural assignments for the closed-shell $(Al_2O_3)_n(AlO)^+$ cluster ions, with n=1,2, and 4, and for $(Al_2O_3)_4^+$ is given by comparing experiments and DFT calculations. In all cases good agreement is found with the global minimum structures. Two dimensional curved structures are found, which are completely different from any known bulk-like or "chemical intuition" structure. They were only found because of the genetic algorithm which allows to extend the search for the global minima to a much larger class of possible structures.

It is shown that all previous calculations or assumptions on the $(Al_2O_3)_4^+$ structure were inadequate. Only after the IR spectra were measured by IR photodissociation spectroscopy the global optimization technique based on genetic algorithm could be tested, finding the global minimum structure of $(Al_2O_3)_4^+$.

The structures found are based of hexagons consisting of alternating Al and O atoms. Every pair of neighboring hexagons share two or three atoms. Two hexagons sharing three atoms induce the curvature of the two-dimensional structures. This hexagon network, which grows with cluster size, has as perimeter a ring of alternating Al and O atoms. With increasing number of atoms, the size of the perimetric ring increases. The evolution of the structure with cluster size can be followed spectroscopically observing that the most intense absorption band is due to vibration modes of atoms from the perimetric ring. The larger the ring, the higher are the vibrational frequencies.

At larger cluster sizes the observed open cage structures may close and/or bulk-like structures may appear. Therefore, it will be interesting to explore larger aluminum oxide clusters in future experiments looking for such characteristic structural changes with cluster size. Moreover, one may try to reduce the curvature radius of the observed structures by doping the cluster with a different element, since a space tessellation based on hexagons is by itself not the most convenient to induce cage structures.